Measurements of the Total Water Content of Cirrus Clouds. Part I: Instrument Details and Calibration

E. M. WEINSTOCK, J. B. SMITH, D. SAYRES, J. R. SPACKMAN,* J. V. PITTMAN,+ N. ALLEN, J. DEMUSZ, M. GREENBERG, M. RIVERO, L. SOLOMON, AND J. G. ANDERSON

Department of Chemistry and Chemical Biology, Harvard University, Cambridge, Massachusetts

(Manuscript received 10 May 2005, in final form 23 March 2006)

ABSTRACT

This paper describes an instrument designed to measure the sum of gas phase and solid phase water, or total water, in cirrus clouds, and to be mounted in a pallet in the underbelly of the NASA WB-57 research aircraft. The ice water content of cirrus is determined by subtracting water vapor measured simultaneously by the Harvard water vapor instrument on the aircraft. The total water instrument uses an isokinetic inlet to maintain ambient particle concentrations as air enters the instrument duct, a 600-W heater mounted directly in the flow to evaporate the ice particles, and a Lyman-α photofragment fluorescence technique for detection of the total water content of the ambient air. Isokinetic flow is achieved with an actively controlled roots pump by referencing aircraft pressure, temperature, and true airspeed, together with instrument flow velocity, temperature, and pressure. Laboratory calibrations that utilize a water vapor addition system that adds air with a specific humidity tied to the vapor pressure of water at room temperature and crosschecked by axial and radial absorption of Lyman-α radiation at the detection axis are described in detail. The design provides for in-flight validation of the laboratory calibration by intercomparison with total water measured by radial absorption at the detection axis. Additionally, intercomparisons in clear air with the Harvard water vapor instrument are carried out. Based on performance of the Harvard water vapor instrument, this instrument has the detection capability of making accurate measurements of total water with mixing ratios in the mid- to upper troposphere of up to 2500 ppmv and mixing ratios in the lower stratosphere of about 5 ppmv, corresponding to almost three orders of magnitude in measurement capability.

1. Introduction

Accurate measurements of the ice water content (IWC) of cirrus clouds are required for understanding their radiative properties, their impact on the water vapor budget of the upper troposphere and lower stratosphere, and for validation and calibration of satellite-borne instruments that measure cloud properties (Stephens et al. 2002). The critical need for accurate measurements of cloud IWC is succinctly summarized in a statement by the Intergovernmental Panel on Climate Change (IPCC): "As has been the case since the first IPCC report in 1990, probably the greatest uncertainty in future projections of climate arises from clouds and their interactions with radiation" (Stocker et al. 2001). Toward this end, general circulation models bear the brunt of the prediction responsibility, and the greatest source of uncertainty within these models is the characterization of cirrus clouds. Furthermore, "the weakest physical link for the representation of microphysical and radiative processes in cloud- and larger-scale models are connected descriptions of the microphysical and radiative characteristics" (McFarquhar et al. 2002).

Accurate measurement of the IWC associated with optically thin cirrus clouds potentially involved in the dehydration process is critical for understanding the mechanisms that control entry-level stratospheric water vapor. For example, if a cirrus cloud forms as an air parcel is cooled, total water remains constant while water vapor decreases. On the other hand, if the source of a cirrus cloud is an anvil, there is no constraint on the total water in the cirrus cloud relative to the water vapor in the surrounding cloud-free air. As a result, the

* Current affiliation: Chemical Sciences Division, NOAA/Earth System Research Laboratory, Boulder, Colorado.

+ Current affiliation: University Space Research Association, NASA Marshall Space Flight Center, Huntsville, Alabama.

Corresponding author address: Dr. Elliot Weinstock, Department of Chemistry and Chemical Biology, Harvard University, 12 Oxford Street, Cambridge, MA 02138.
E-mail: emweinstock@yahoo.com

conservation of total water in the cloud and in clear air along the isentrope at which the cloud is sampled can help distinguish a cloud formed in situ from one resulting from anvil formation.

We describe here a new instrument that combines an isokinetic inlet, a heated duct, and photofragment fluorescence detection for the quantitative measurement of the total water content of a cirrus cloud. In this manuscript, we also detail the laboratory calibrations that are central to the accuracy of both the water vapor and total water measurements. In the accompanying paper, Weinstock et al. (2006, hereafter Part II), we describe results from test flights on the National Aeronautics and Space Administration (NASA) WB-57 research aircraft, from the Clouds and Water Vapor in the Climate System mission (CWVCS) based out of San Jose, Costa Rica, in the summer of 2001, and the Cirrus Regional Study of Tropical Anvils and Cirrus Layers Florida Area Cirrus Experiment (CRYSTAL FACE) based out of Key West, Forida, in July 2002.

The total water instrument utilizes the same module for detecting ambient water as the Harvard water vapor instrument (Weinstock et al. 1990, 1994; Hintsa et al. 1999), but a different inlet. The instrument needs to deliver ambient air to the detection module in which ambient ice particles have been fully evaporated, while avoiding contamination from instrument walls. In principle, it can be designed to be either isokinetic, thus maintaining ambient ice particle number densities, or anisokinetic, with enhancement factors calculated using measured instrument and ambient mass flow rates, and measured particle size distributions. In cloud-free air, both the total water and water vapor instruments should identically measure ambient water vapor, and the agreement represents a first-order requirement for validating in flight the accuracy of a total water instrument detection method. Because the two instruments operate in different flow regimes and at different temperatures, this criterion actually poses a strict test on the data quality of both instruments. For the total water instrument, it specifically provides a sensitive test for wall contamination or hysteresis from surfaces in the inlet and instrument duct. For the water vapor instrument, it confirms the lack of dependence of detection sensitivity on temperature. Attention to accuracy is critically important since recent history indicates that validating the accuracy of water vapor instruments remains challenging (e.g., Kley et al. 2000).

2. History of total water instruments

There have been only a few instruments developed to measure total water in the upper troposphere (UT) and lower stratosphere (LS), and details of inlet and heater design are often unpublished. Kelly (1993) utilized a pair of Lyman-α photofragment fluorescence hygrometers with forward- and rear-facing inlets contained within an aerodynamically shaped pod (football) suspended from the fuselage of the NASA ER-2 research aircraft. Brown (1993) and Brown and Francis (1995) used a total water probe that combines a heated isokinetic inlet and Lyman-α absorption to measure total water on a Met Office C-130 aircraft. Schiller et al. (1999) reported results from a total water instrument on board the Deutsches Zentrum fur Luft- und Raumfahrt (DLR) Falcon research aircraft. The instrument is a modified version of the Fast In Situ Hygrometer (FISH) instrument (Zöger et al. 1999) that utilizes Lyman-α photofragment fluorescence detection and an inlet with anisokinetic flow to enhance sensitivity to low ice water. Similarly, Avallone has developed a total water instrument, a Closed Path Tunable Diode Laser Hygrometer (CLH; Avallone and Hallar 2003; Hallar et al. 2004), which flew on the NASA DC-8 research aircraft during the Stratospheric Aerosol and Gas Experiment (SAGE) Ozone Loss Validation Experiment (SOLVE) in 2000, and more recently on the WB-57 aircraft during CRYSTAL FACE. The instrument uses a single-pass Infrared Diode Laser Spectrometer for detection (May-Comm Instruments, LLC), a heated inlet, and anisokinetic flow to enhance sensitivity to thin ice clouds. Webster et al. (2003) have modified the Aircraft Laser Infrared Absorption Spectrometer (ALIAS; Webster et al. 1994) with a heated isokinetic inlet for the measurement of total water and its isotopes on the WB-57 aircraft. In principle, the enhancement factor in anisokinetic particle sampling can be calculated and asymptotically reaches a value approximately equal to the ratio of ambient and inlet mass flows for particles larger than about 20 μm (see Hallar et al. 2004). However, for the range of particle sizes that the total water instrument was designed for, calculated enhancement factors may have large uncertainties. Additionally, these uncertainties are exacerbated by the large uncertainties in the size distribution of these small particles.

While all the aforementioned instruments measure total water, one instrument, using a counterflow virtual impactor for particle sampling (Twohy et al. 1997), directly measures cloud ice and/or liquid water content. This instrument has previously flown on the National Center for Atmospheric Research (NCAR) Electra and Cessna Citation operated by the University of North Dakota, with peak altitudes of about 13 km. It has been integrated onto the WB-57 for cloud studies as well as intercomparison with the previously described total water instruments.

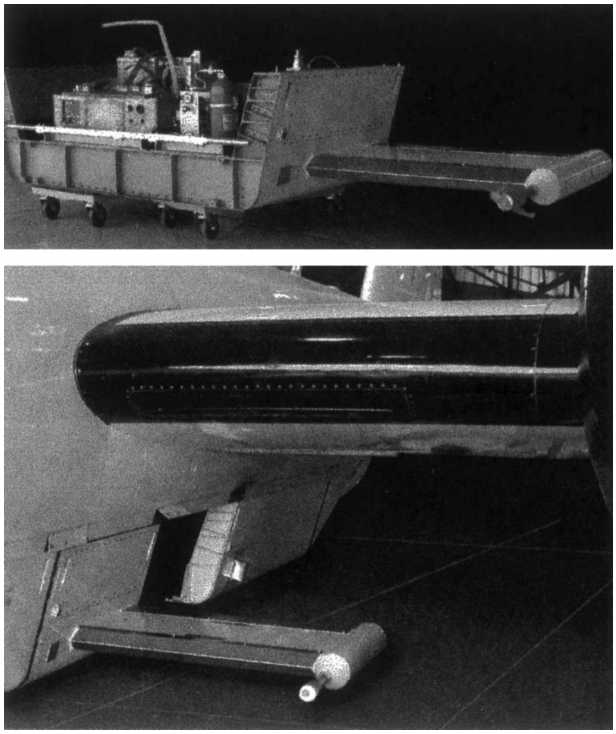

FIG. 1. The total water instrument in-flight configuration mounted in the WB-57 pallet (top) in preparation for a flight at the NASA Johnson Space Flight Center and (bottom) in the aircraft.

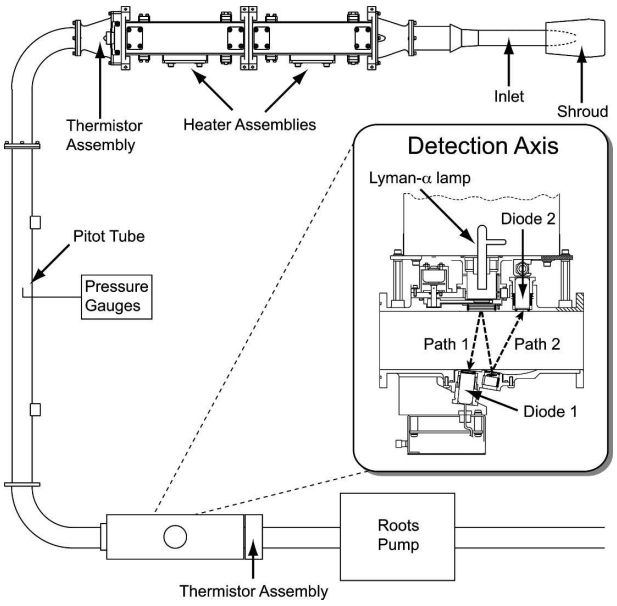

FIG. 2. A schematic representation for measuring total water by photofragment fluorescence. The detection axis illustrates the Lyman-α lamp, absorption paths, and photodiodes. The photomultiplier and associated optics for fluorescence detection that sit at right angles to the exciting light and airflow are not shown here. Relevant dimensions are shown in cm for lengths along the flow from the inlet tip to the detection axis.

3. Total water instrument details

The total water instrument was designed to fit into a 1-m-wide pallet that is hoisted in place to become part of the underbelly of the WB-57 fuselage. As shown in Fig. 1 (top), the instrument occupies about 60% of the space in the pallet. It weighs 110 kg, with average and maximum power requirements of 750 and 1200 W of 28 V dc power and 600 and 800 W of 110 V ac power, respectively.

Figure 1 (bottom) illustrates the location of the inlet, which extends a meter out from the edge of the pallet that is 1.83 m across. As pictured, the front of the inlet is about a meter below and 10 cm forward of the leading edge of the aircraft wing. The inlet is firmly supported by weldments that are attached to struts at the bottom of the pallet. An aerodynamically designed aluminum clamshell is bolted to the inlet and the entire assembly is sealed with a low-temperature RTV silicone sealant. As pictured in Fig. 1 (top) for the initial test flights and the CWVCS mission, the pallet also contains the Harvard ozone instrument.

As illustrated schematically in Fig. 2, the total water instrument can be divided into four subsystems.

1) A carefully designed and positioned inlet through which ice particles are brought into the instrument duct such that the quantitative relationship between ambient ice water content and sampled ice water content of air is determined to better than 15% for particle sizes up to 100 μm in diameter.
2) A heater designed to evaporate solid/liquid water before it reaches the detection axis.
3) Ducting through which the air flows to the detection axis without perturbing the ambient total water mixing ratio.
4) A detection axis that accurately and precisely measures the total water content of the ambient air.

The accuracy of the instrument depends on how well the instrument performs each of the four functions described above. Instrument uncertainty, discussed below, can be determined by properly combining the uncertainties in the performance of each of those functions. We discuss each of these instrument subsystems separately.

4. The inlet

There are four basic considerations for designing the inlet for quantitative particle sampling: 1) the proper-

ties of the walls and surfaces within the inlet and instrument ducts, 2) the position of the inlet relative to the aircraft skin, 3) the inlet shape, and 4) the angle of attack. Regarding the first of these, water vapor molecules have a propensity to stick to surfaces, introducing an increased time constant or hysteresis in the measurement. To reduce this problem, the interior walls of the aluminum inlet and ducting from the inlet to the detection axis are coated with FluoroPel (Cytonix Corporation), a hydrophobic coating. The ultimate questions for the last three design criteria are, how do the trajectories of particles entering the inlet vary as a function of particle shape and size, and how will perturbations of particle trajectories affect the relationship between the sampled particle concentration and that in the ambient airstream? In all cases the momentum of the particle tends to keep it moving in a straight line even as the gas streamlines are bending to avoid obstructions such as the aircraft fuselage or the inlet nose. Design criteria, used to best locate the inlet relative to the WB-57 fuselage, are based on a series of studies by King (1984, 1985). Computional Flow Dynamics (CFD) calculations that model particle enhancement at representative inlet positions around the WB-57 (Engblom and Ross 2003) are also used to evaluate particle enhancement characteristics at the inlet. While the CFD model studies do not specifically consider particle sampling questions for the exact location of our total water inlet, conclusions can be drawn from the enhancement factors calculated for two of the chosen inlet positions.

Theoretical and experimental studies of airflow and particle trajectories around aircraft fuselages (King 1984; King et al. 1984) have shown that for a range of aircraft, aircraft velocities, and ambient pressures, enhancement factors depend on a modified Stokes number S where $S = 2a^2v\rho_p/9\upsilon r$, and d/r, the ratio of the inlet distance from the fuselage to the fuselage radius. Here, a is particle radius, v is flow velocity, r is fuselage radius, ρ_p is particle density, and υ is the viscosity of the air. The enhancement factor can be calculated for values of S up to 6 (corresponding to maximum enhancement), using empirical equations from King (1984). We plot in Fig. 3 (left) particle enhancement factors for a fuselage radius of about 1 m and a value of $d/r = 1$, as a function of S. With $d/r = 1$, or a 1-m distance from the aircraft skin, particles can be measured with an enhancement of 6% or less. Figure 3 (right) illustrates the enhancement as a function of d/r for $S = 6$.

Calculations have also been carried out (King 1985) for ice particles of variable shape and ice density, with results consistent with those assuming spherical water drops: dependence of the enhancement factor on a modified Stokes number is independent of particle

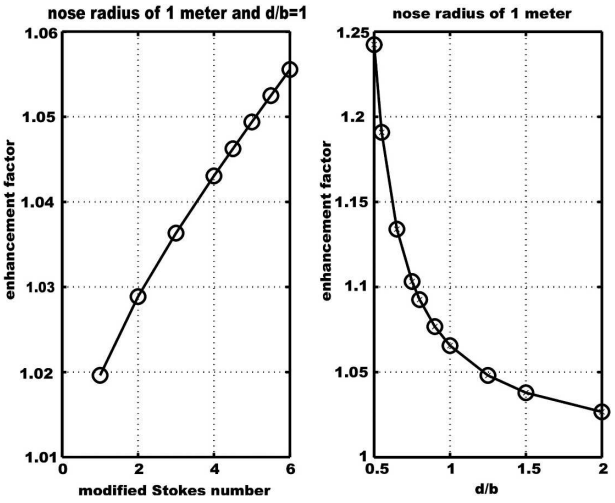

FIG. 3. Plots illustrating the efficiency of measuring particle concentration on the inlet designed for the WB-57. (left) The particle enhancement factor is plotted vs the modified Stokes number. (right) The variation of enhancement factor is shown as a function of inlet distance from the aircraft divided by the aircraft radius for $S = 6$, corresponding to 50-μm diameter particles.

shape. However, the enhancement factor does depend on ice density, which is typically not well known for large ice particles. Further uncertainties in these estimates resulting from the shape of the WB-57 fuselage as well as the limitations to the enhancement factor calculation for Stokes numbers less than 6 can also be addressed by the recent CFD calculation of Engblom and Ross (2003). In their study, they calculate ice particle enhancement factors at four representative inlet positions around the WB-57. Two of the pallet positions represent extremes for inlets at pallet position 1, being, respectively, 30.5 and 175 cm from the fuselage. At these locations, the model tests the sensitivity of ice particles reflecting off the fuselage and wing into the inlet. For the modeled inlet position close to the fuselage, enhancements can reach a factor of 2 for 200-μm-diameter particles, tailing off to about 1.6 for particles upward of 600-μm diameter. However, as the authors of the study note, at WB-57 airspeeds, large ice particles are known to shatter on impact (Engblom and Ross 2003; Hallett and Isaac 2002), and the resulting smaller particles are not expected to enhance the particle signal at this inlet. We believe that because the total water inlet is positioned 3 times farther from the fuselage than the modeled inlet in the CFD study, enhancements from ice bouncing off the fuselage should not be a problem, even for large particles. Nevertheless, it is beyond our capabilities to estimate what the enhancement might be. While, without further CFD calculations we can neither quantify it, nor a priori rule it

out completely, we outline in Part II in-flight data intercomparisons that shed light on this issue.

The requirement of isokinetic flow means that the mass flow through the inlet must be identical to the corresponding ambient mass flow through the identical cross-sectional area. Mass flow in the inlet is determined using Bernoulli's equation where the local flow speed $V = \sqrt{2(p_0 - p)/\rho}$, where p_0, the stagnation pressure, and p, the static pressure, are both measured by a pitostatic tube (United sensor PCC-12-KL) as shown in Fig. 2, and ρ is the density of air. Matching mass flow within the instrument to the ambient mass flow requires adjusting for the velocity where the Pitot tube is mounted in the 2.86-cm-diameter flow tube relative to that at the 1.1-cm-diameter inlet entrance. With a nozzle inner diameter of 1.1 cm, the velocity through the 5.08-cm square cross-section detection axis will be about 5–6 m s^{-1} when the flow is isokinetic, depending upon the true airspeed of the WB-57. A roots pump is used to both regulate this velocity in response to changes in altitude and velocity, and scan flow velocity for diagnostic purposes. The control circuitry for the roots pump uses the pressure, temperature, and true airspeed as supplied from aircraft navigation data to set the pump rpm. Measurement error is proportional to the anisokinetic factor A, defined as the ratio of the integrated mass flow through the 1.1-cm inner diameter cross-section inlet to the mass flow of the free airstream through a comparable cross-sectional area, where oversampling (undersampling) with $A > 1$ (<1) leads to an under- (over) determination of IWC.

The errors incurred in establishing isokinetic flow are threefold. The first is in our measurement of the mass flow within the inlet. The relationship between differential pressure and mass flow was determined for well-developed flow over a wide range of pressures and flow velocities using a 400 standard liters per minute (slm) (MKS Instruments) flow controller with a statistical uncertainty of 5%. The duct pressure is measured using a 1000 torr Baratron (MKS Instruments) to 1% or better, and thermistors at the detection axis illustrate that duct temperatures are homogeneous to ±5°, thus providing an additional 2% uncertainty in the density of air in the duct and accordingly in the determination of mass flow within the duct.

The second source of error is in the ambient mass flow and is based on the uncertainties in the true airspeed, pressure, and temperature that are measured by the aircraft navigational system, and the assumption that these are suitable substitutes for the actual airspeed, pressure, and temperature at the inlet. Based on intercomparisons with measurements by the Meteorological Measurement System (Scott et al. 1990), uncertainties in the aircraft pressure, temperature, and true airspeed measured by the aircraft navigational system are 2%, 1%, and 2%, respectively. When combined with the uncertainty in the determination of mass flow within the duct, this results in a total uncertainty of 6.2% in the establishment of the duct velocity necessary to provide isokinetic flow. Additionally, we use values from Table 4 in Engblom and Ross to estimate the uncertainty in the ambient true airspeed and pressure at our inlet. Using the inlet position that gives the larger deviations from aircraft navigational values for angles of attack of 2° and 6°, we estimate that the Mach number at the inlet is reduced relative to the aircraft by 5% and 15%, respectively. Consistent with the inlet being located almost a meter below the aircraft wing, the CFD-modeled pressure is increased by 2% and 6%, respectively, relative to the navigational system measurements. The combination of these two effects suggests that the mass flow in the inlet, for these angles of attack, is approximately 3% and 9% too high, resulting in an undersampling of particles. However, the 6° angle of attack occurs during steep aircraft ascents, typical during climbout, with a corresponding negative angle of attack during steep descents typically prior to landing. During most cloud studies, the aircraft is flying at a relatively constant altitude in order to remain within the cloud, where the aircraft angle of attack is approximately 2°.

The third source of error is in the assumption that we are establishing isokinetic flow at the inlet entrance through the measurement of average flow properties within the instrument duct. The sampling sensitivity to particles approaching the edge of the inlet will be affected. A simple calculation of the uncertainty this causes can be made by assuming that particles in a cross-sectional area defined by a 1-mm-wide annulus at the wall will be affected, corresponding to 30% of the total cross section of the inlet. Conservatively assuming an additional 30% uncertainty in the sampling efficiency in the inlet for these particles based on flow inhomogeneities, the overall increase in the uncertainty on the establishment of isokinetic flow will be proportional to the fraction of the inlet tube cross-sectional area affected, or about 9%.

The National Advisory Committee for Aeronautics (NACA) 1–55–100 inlet shape was successfully used for the inlet to the ClO instrument (Soderman et al. 1991) on the NASA ER-2 research aircraft that flies at Mach 0.7, and is used for the 1-cm inlet. It has been demonstrated by wind tunnel tests that to avoid flow separation or measurement enhancements it is necessary to attack the streamlines within an angle of 1°–2°. As shown in the wind tunnel test of Murphy and Schein

TABLE 1. Sources of particle sampling uncertainty in the total water instrument.

Source of uncertainty	Uncertainty (%)
Average isokinetic flow	±6.2
Calculated particle enhancement (King 1984)	+6.0
Angle of attack = 2°	−3.0
Angle of attack = 6°	−9.0
Isokinetic flow inhomogeneities	±9.0
Total uncertainty	±15.0

(1998), a shroud around the inlet allows flow at the inlet entrance to be significantly less sensitive to this angle. For our inlet, the shroud has a 7.6-cm inner diameter and is scaled directly from the inlet used by Murphy and Schein. Using Rader and Marple [1988, their Eq. (17)], we calculate that the sampling efficiency scales inversely and approximately linearly with absolute value of the mass flow ratio, with a ratio of 1.1 (or 0.9) giving a 10% undersampling (or oversampling). Accordingly, depending on aircraft angle of attack, we estimate a –3.5% enhancement from flow perturbations at the inlet under most conditions. However, there is an additional contribution to the uncertainty when the aircraft is changing altitude.

We summarize in Table 1 the sources of particle sampling uncertainty in the total water instrument. The particle enhancement of 6% as shown in Fig. 3 acts in opposition to the –3.5% enhancement resulting from the aircraft angle of attack based on CFD calculations. However, we do not have enough confidence in these results to treat them as systematic errors that cancel. Rather, we account for these two competing effects by adding 10% to the uncertainty in particle enhancement. By combining that 10% enhancement with the 6.2% uncertainty in the equation that sets the conditions for isokinetic flow and the 9% uncertainty from flow inhomogeneities, we get a total uncertainty of 15% in particle sampling efficiency.

5. The heater

The total water instrument was designed primarily for measuring the ice water content of thin cirrus in the tropopause region. Accordingly, the heater design was predicated on the need to completely vaporize particles within the transit time from the heater to the detection axis, or about 160 ms when the aircraft airspeed is 150 m s^{-1}. We make the assumption that the equivalent of a 100-μm-diameter spherical ice particle represents the largest particle that the instrument would need to evaporate in the upper tropical troposphere and tropopause region. Based on that assumption, a 30°C duct temperature is required. A 600-W heater is needed to raise the air temperature to the prescribed 30°C from typical ambient temperatures in the upper troposphere and lower stratosphere. The heater consists of two 300-W assemblies that are wired in parallel and constructed of strips of nichrome ribbon (California Fine Wire Stableohm 650, 0.004″ thick, 0.25″ wide, with a resistance of 0.55 ohms ft^{-1}) mounted axially in the flow tube using machinable glass ceramic mounts and providing extremely efficient heat transfer to the airstream. The assemblies are mounted in a 3.18-cm inner diameter section of the flow tube as shown in Fig. 2. A set of three thermistors just downstream of the heater monitor the air temperature with the center thermistor providing a signal used in a feedback loop by a pulse-modulated heater controller that maintains the air temperature stable to better than a degree. While the three thermistors indicate a temperature gradient between the wall and the center of the tube of about 10° cm^{-1}, it is the temperature of the core that is most important. This is because while the ducting expands from the initial 1-cm inner diameter of the inlet to a 5-cm rectangular cross section at the heater, the trajectories of the larger particles are preferentially maintained in the central core of the flow. While the walls of the instrument are heated and insulated, there are axial and radial temperature gradients within the instrument duct, with the air temperature gradually cooling as it flows toward the detection axis. There, the minimum temperatures adjacent to the colder walls approach 10°C and the temperature gradient across the flow tube is about 5°–10°C. This temperature is well above saturation even when ice in the thickest clouds encountered is evaporated in the instrument.

During the CRYSTAL FACE campaign, we encountered cirrus clouds with particle diameters up to 1 mm, significantly larger than the 100-μm diameter the instrument was designed to evaporate. While the potential of incomplete evaporation of large particles is significant, especially based on evaporation times for these particles in a duct maintained at 30°C, the actual temperature of the core of the flow as it passes through the 30-cm-long heater is much higher than the duct temperature. We first illustrate in Fig. 4 the evaporation time in the duct as a function of water equivalent diameter, using Eq. (13.19) from Hinds (1999). We believe these evaporation times are somewhat conservative because cirrus ice particles are nonspherical, have a higher surface-to-volume ratio than a sphere, and an effective ice density lower than the actual density of ice. In the top panel we see that evaporation times are well in excess of the 160-ms residence time of the instrument, but it is also noteworthy that by raising the temperature to 60°C we can fully evaporate particles with a

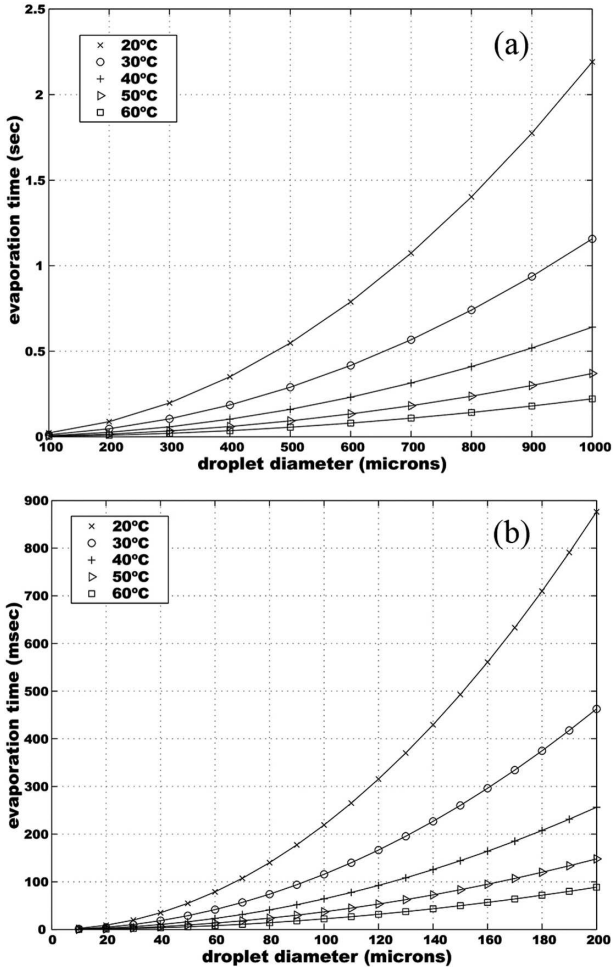

FIG. 4. Evaporation times plotted as a function of duct temperature for various particle sizes (a) up to 1000-μm diameter and (b) up to 200 μm.

water equivalent diameter of about 250 μm within 160 ms. This temperature increase will represent the simplest change in instrument operation for future missions in which thick cirrus will be sampled. As mentioned in Part II, the addition of a 50-μm mesh stainless steel screen between the two heater sections ensures the breakup and complete evaporation of ice particles larger than the upper limit suggested by the evaporation times plotted in Fig. 4. However, during the CRYSTAL FACE mission, the scattered light observed at the detection axis during thick cloud encounters was indicative of residual ice particles. While comparisons with the much larger scattered light signal in the nearly identical water vapor detection axis suggest that a very small amount of ice remained unevaporated, it cannot be quantified. During the following missions, the stainless steel screen reduced this signal to negligible levels.

a. The roots pump

Laboratory pressure drop tests through a prototype total water instrument indicated that the use of aircraft ram pressure would be insufficient to maintain isokinetic flow. A roots pump was chosen because of its capability of pumping a great deal of air without needing to maintain a significant pressure drop. The Eaton Supercharger Model 45 (Magnuson Products, Ventura, California) was chosen in part because of its previously successful use at low pressure (D. Toohey 1996, personal communication). The pump was typically run between 2000 and 3000 rpm providing a displacement of about 40 to 60 cubic feet per minute (cfm). The pump is controlled by a combination Parker NO342FENMSN brushless servomotor and Parker Automation Gemini GVU3 120/240 VAC digital servo controller. The rpm of the pump is actively controlled using an algorithm that calculates required mass flow from the aircraft navigational system pressure, temperature, and true airspeed, and the total water instrument duct temperature, pressure, and flow velocity.

b. The detection axis

The detection axis is functionally identical to that in the water vapor instrument that has been previously described in detail (Weinstock et al. 1994). A simple diagram is shown as part of Fig. 2. Briefly, 121.6-nm (Lyman-α) radiation from a radio frequency (RF) discharge lamp photodissociates water vapor in a 5.08-cm duct. A fraction of the resulting OH fragments are formed in their first excited electronic state ($A^2\Sigma^+$), and the OH fluorescence at ~315 nm is collected at right angles to the Lyman-α beam through a narrowband filter and detected with a photomultiplier tube (PMT). As shown in Weinstock et al. (1994), the normalized fluorescence signal can be expressed as

$$S = C_0 Q[H_2O], \tag{1}$$

where C_0 is the calibration factor at zero air density, $[H_2O]$ is the water vapor concentration, and Q is the quenching coefficient that depends on the density of air M,

$$Q = \frac{1}{1 + q_{\text{air}} M}. \tag{2}$$

At altitudes of the upper troposphere and lower stratosphere, $q_{\text{air}}M$ is much larger than 1, and the observed detector signal is directly proportional to $[H_2O]/M$, the water vapor volume mixing ratio. Lamp scatter near 315 nm, the source of the background counts detected by the PMT, is measured by using a quartz window that periodically blocks the Lyman-α beam.

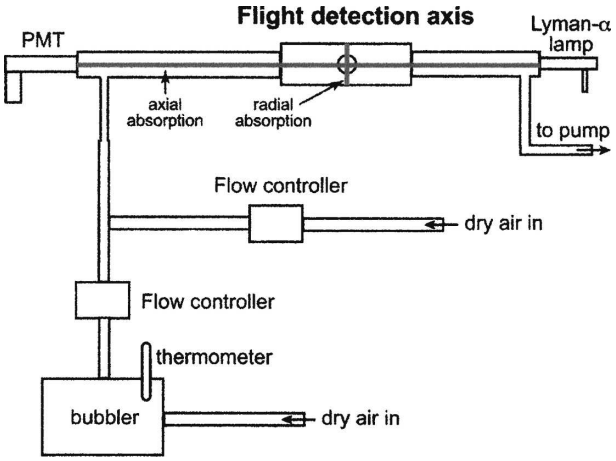

FIG. 5. A schematic representation of the laboratory calibration facility.

Changes in lamp intensity are monitored with a vacuum photodiode opposite the lamp and are used to normalize the fluorescence signal. Additionally, a 2.54-cm focal length, 1.27-cm-diameter magnesium fluoride mirror, rear-surface coated for the vacuum ultraviolet, is used to reflect a portion of the Lyman-α beam back across the tube to a second photodiode, providing the means to carry out radial absorption measurements in the laboratory and in flight when the water vapor concentration is sufficiently high, typically in the mid- to upper troposphere.

6. Instrument calibrations

The pre- and postmission laboratory calibrations are carried out for the water vapor and total water instruments by measuring fluorescence over a range of pressures and water vapor mixing ratios, using the calibration setup schematically represented in Fig. 5. The added water vapor mixing ratio, WV_{bub}, is calculated using Eq. (3),

$$WV_{bub} = \frac{[H_2O]}{M} = \frac{P_{H_2O}}{P_B} \cdot \frac{\phi_h}{\phi_h + \varphi_d}, \qquad (3)$$

where P_{H_2O} is the vapor pressure of water at the bubbler temperature, P_B is the total pressure measured at the bubbler, and ϕ_h and φ_d are the flow rates of humidified and dry air, respectively. The humidified airflow is typically 1%–2% of the dry airflow. The calibrations explore both a wide range of water vapor mixing ratios (20–500 ppmv) and pressures (20–300 mb) in order to determine the instrument calibration and validate its linearity throughout the full range of mixing ratios that are reported during a flight. For calibrations that utilize water vapor concentrations greater than 2×10^{14} molecules per cubic centimeter, the water vapor mixing ratio can be measured directly by radial absorption of Lyman-α radiation. For calibrations carried out after the CRYSTAL FACE mission, water vapor was simultaneously measured by axial absorption of Lyman-α radiation as well.

The calibration constants that are used for the measurement of total water during the flights described in the accompanying validation paper are determined from the calibration runs that are shown in Fig. 6. These calibration constants are determined from a least squares fit to the points plotted in red in the figure, for which the added water vapor mixing ratios were calculated based on the bubbler vapor pressure. Uncertainties of 0.1° in the bubbler temperature result in a 0.7% uncertainty in the partial pressure of water vapor. Additional uncertainties are 0.3% in the total pressure at the bubbler, and 1% in the ratio of the flow rates based on calibration of these sensors. For the mixing ratio determination, the uncertainties in flow tube temperature of 0.3% and flow tube pressure of 0.5% must be added. These uncertainties combine to yield a total 1-σ statistical uncertainty in the water vapor mixing ratio of 1.5% from Eq. (3). Additional uncertainty arises from the standard deviation in the slope in the plot of 1/C versus M, typically 2% or better. A 3% 1-σ uncertainty in the water vapor mixing ratio results from combining the statistical uncertainty from Eq. (3) with the 2% uncertainty in the derived slope. This 3% uncertainty is consistent with the 3% 1-σ uncertainty in the Lyman-α cross section from Kley et al. (1984) that leads to a 3.5% (axial absorption) uncertainty in the water vapor mixing ratio determined from the absorption methods described below.

Plotted as well in the figure are the points in green for which added water vapor is determined from radial absorption of Lyman-α radiation. Note here that the calibration constants determined by the two independent methods agree to within 2%. This agreement sets the criteria for establishing the maximum systematic difference between the calibration constants determined using the water vapor mixing ratio calculated from Eq. (3) and those determined using Lyman-α absorption at the detection axis. Accordingly, this agreement quantifies the potential errors from hysteresis effects during calibration that result in systematic differences between the water vapor mixing ratios supplied by the bubbler and Eq. (3) and those at the detection axis. Thus we add an additional uncertainty of 2% to incorporate the maximum allowable difference between detection sensitivities derived from calibrations using Eq. (3) and those using Lyman-α absorption,

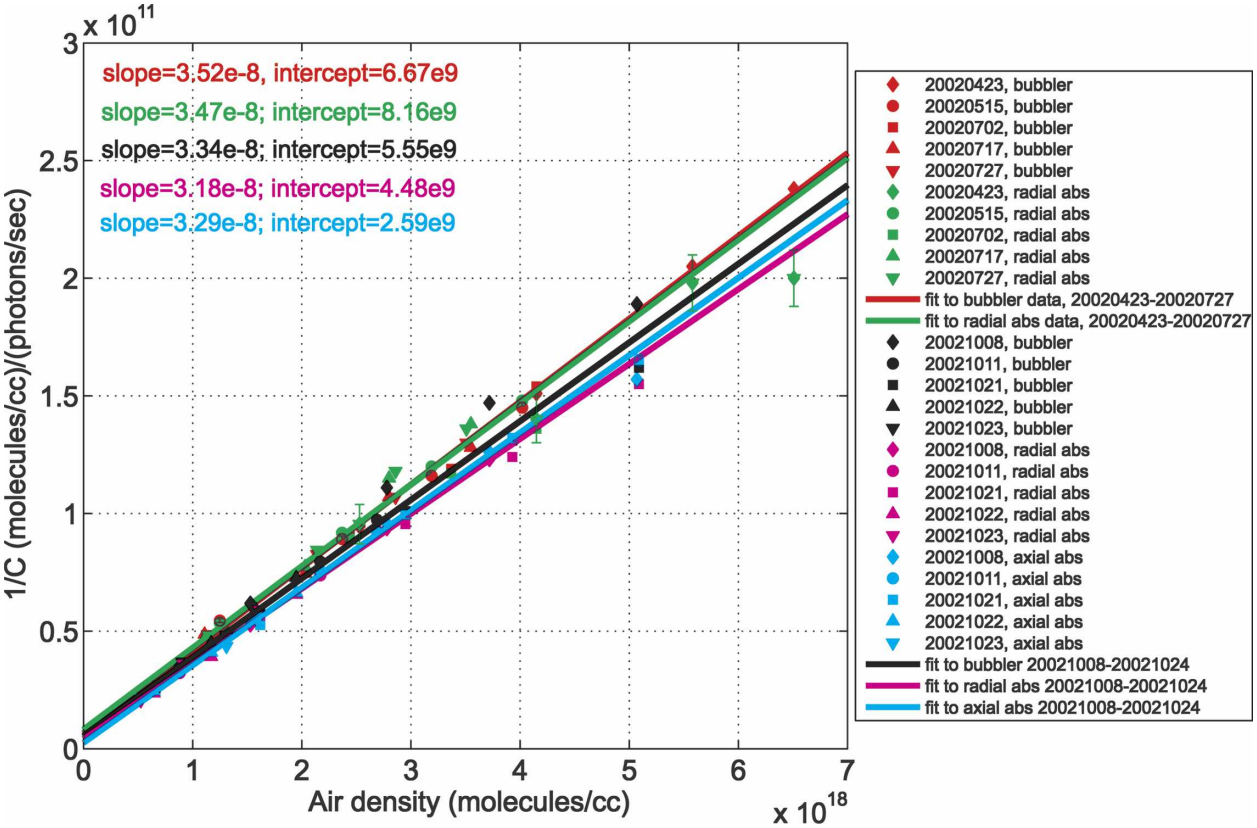

FIG. 6. Plot illustrating calibration data applicable to the data taken during the CRYSTAL FACE campaign. The first date corresponds to the last calibration run taken at Harvard. The next four runs were all carried out in the field, and the remainder at Harvard after the CRYSTAL FACE mission. The slopes and intercepts are color coded to correspond to the data and the lines for each calibration run.

yielding a total 1-σ uncertainty of 5%. However, we acknowledge that during missions designed to study clouds [e.g., CRYSTAL FACE and the Midlatitude Cirrus Experiment (MidCiX)], deterioration in the transmission of the window of the photodiode that monitors lamp flux is possible, systematically increasing instrument sensitivity. Under these circumstances, intercomparisons between water vapor and total water in clear air and in-flight absorption measurements help identify optical degradation events.

An axial absorption axis was permanently installed into the calibration facility after the CRYSTAL FACE mission, and the remainder of the calibration runs plotted in Fig. 6 illustrate comparisons of calibration constants derived simultaneously using the three described methods. The 5% difference between the calibration constants determined from the postmission calibrations using, respectively, WV_{bub} and water vapor determined from radial absorption is caused in part by the lower water vapor concentrations used in those runs, making the short-path radial absorption measurement more prone to systematic errors. The representative error bars included in Fig. 6 illustrate the larger uncertainty in the radial absorption data. While representative error bars for the other data are included, they are about a factor of 5 smaller than those for the radial absorption data and accordingly difficult to see. The agreement between the calibration constants derived from WV_{bub} and that from axial absorption is 1.5%. The difference between the mission and postmission calibration constants of about 5% is attributed to deterioration of the transmissivity of the vacuum ultraviolet photodiode that monitors Lyman-α intensity. These deposits are also observed on the detection axis walls that were painted black to minimize scattered light. Uncertainties in the instrument calibration constants resulting from calibration changes observed during postmission calibration runs have prompted the implementation of laboratory calibrations in the field.

To describe in more detail how each data point in Fig. 6 is derived, we plot in Fig. 7 measured fluorescence counts for an entire calibration run. Four dry-airflow settings are delineated in the figure, corresponding to groupings of measurements made at four

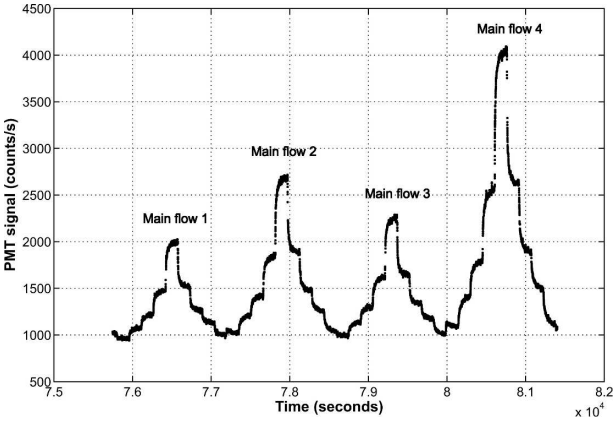

FIG. 7. Plot of PMT signal during a calibration run. Each calibration run is divided into four pressure regions, determined by the setpoint of the dry-airflow controller. The bubbler flow controller is varied in stepwise fashion from no flow, to a maximum flow, and then back to no flow.

air densities. At each air density, the humidified-airflow controller is varied in stepwise fashion from no flow, to peak flow, and then back to no flow. A plot of photomultiplier signal versus added water at each of these air densities yields a straight line with a slope equal to the sensitivity to water vapor at that air density in PMT signal (counts per second)/(molecules per cubic centimeter). The slope at each value of M provides a calibration point as plotted in Fig. 6. The intercept corresponds to the signal when there is no flow through the bubbler and results from the humidity of the dry air along with any residual water coming off the walls. While the dry air we use typically contains less than 5 ppmv water, as long as its water content remains relatively constant, its value has no effect on the calibration. Each data point in Fig. 6 corresponds to the slope of a least squares fit of normalized PMT signal versus water added at the measured air density. The water added can be calculated using Eq. (3), or determined simultaneously from the absorption of Lyman-α radiation using radial or axial absorption. Besides the statistical uncertainty from counting statistics in the plotted 8-Hz data, the variability at each flow setpoint illustrates the time for the humidified flow through the system to reach steady state. The calibration constants are determined using data taken only during the last 30 s of each 3-min setpoint setting when the signal has typically stabilized.

The sensitivity of the calibration to differences between laboratory and in-flight detection axis temperatures has been a concern. In flight, the detection axis temperature of the Harvard water vapor instrument is typically about 20°C above ambient, equivalently about 40° to 80°C below room temperature. Potential sensitivity of the calibration to gas temperature exists because OH molecules formed in a range of rovibronic states as a part of the photofragment fluorescence process undergo collisional deactivation. The rate of this process could have a significant temperature dependence that would affect the fluorescence efficiency. For this reason, as described in Weinstock et al. (1994, 1990), laboratory experiments were carried out to verify no significant dependence of the water vapor calibration on duct temperature. Additionally, any uncertainty in the calibration of the total water instrument resulting from air temperature will be virtually eliminated, because the air temperature at the total water detection axis is designed to be near calibration temperatures. In fact, the typical agreement of 3% or better between ambient water vapor measured by the water vapor and total water instruments in flight validates the lack of detection axis sensitivity to temperature.

Agreement between the two instruments also depends upon the stability of their respective calibrations and/or our ability to track each instrument's sensitivity throughout the field mission. The variability or uncertainty in the agreement can also be limited by the signal-to-noise ratio of each instrument, especially at low water vapor mixing ratios. However, optical degradation can combine to simultaneously decrease lamp output and increase background signal from surface scatter and thus lead to either a sudden, or more typically, a steady reduction in each instrument's signal-to-noise ratio during a mission. Furthermore, optical degradation not only decreases instrument sensitivity, but also decreases the transmittance of the photodiode window that monitors the lamp flux, thereby complicating the accurate measurement of that flux. We expect optical degradation of the total water detection axis to be much less than that of the water vapor detection axis because of higher duct temperatures. Accordingly, comparison of the two measurements during a mission provides a means of monitoring the relative stability of their calibrations.

7. Instrument accuracy

This manuscript describes a total water instrument specifically designed to enable accurate measurement of the total water content of thin or subvisible cirrus near the tropical and subtropical tropopause. Because cloud IWC is determined when this measurement is combined with an independent measurement of in-cloud water vapor by our Lyman-α hygrometer, we broaden the assessment of errors here to include the uncertainty in that measurement as well. While the Harvard total water instrument can and often does measure water vapor accurately, the measurement in

TABLE 2. Sources of uncertainty in the measurement of cloud IWC using the water vapor and total water instruments.

Source of uncertainty	Uncertainty (%)
Measurement of total water–water vapor	±7.0
Ice evaporation in water vapor duct	−5.0 maximum
Hysteresis	±5.0 maximum
Particle sampling	±15.0

clear air primarily serves to validate instrument operation, so observed hysteresis in the measurement of water vapor does not directly add to the uncertainty in the total water measurement in clouds. On the other hand, hysteresis in the total water measurement within clouds of course does.

To quantify uncertainties in the total water measurement we define efficiency factors corresponding to the function of the four instrument subsystems described above:

1) inlet particle concentration/ambient particle concentration,
2) particle mass evaporated/duct particle mass,
3) total water at the detection axis/total water entering the duct, and
4) actual sensitivity/sensitivity from calibration.

The total instrument uncertainty results from combining uncertainties in these four efficiency factors. To determine uncertainty in the ice water content measurement requires including the uncertainty in the simultaneous water vapor measurement as well. We list in Table 2 the errors that must be combined to give the total projected uncertainty in the cloud IWC measurement.

We start with item 2, the particle evaporation efficiency in the instrument. The instrument was originally designed for thin cirrus measurements and based on calculations, the results of which are shown in Fig. 4, particles with diameters up to 250 μm will be completely evaporated within the 160-ms residence time in the duct when its temperature is maintained at 60°C. Accordingly, when considering cloud encounters for which this instrument was designed, there is no contribution to uncertainty in the IWC measurement from incomplete particle evaporation.

We next consider the uncertainty corresponding to item 4 in Table 2, the detection axis sensitivity, which as shown previously is ±5%. For the measurement of ice water content, it is ±7%, based solely on the root-mean-square combined uncertainties in the detection axis sensitivities for each of the water instruments. Besides the uncertainty in the calibration, optical deterioration of optical surfaces, and specifically the transmission of the window of the vacuum UV photodiode that monitors lamp flux, can be a source of additional uncertainty. As described in more detail in Part II, this uncertainty is minimized by 1) the intercomparison of the water vapor measurements by the two instruments in clear air, 2) field-based laboratory calibrations as the need arises, and 3) in-flight absorption measurements during transits through high water vapor air. Typically, these strategies have limited this uncertainty to less than 3%. Finally, there is an additional uncertainty resulting from evaporation of ice in the water vapor duct. Based on in-cloud intercomparisons with the JPL hygrometer during CRYSTAL FACE, this evaporation is typically 5% or less.

We next consider the additional error from item 3, which in essence results from hysteresis in the duct. This error as it impacts IWC measurements will be estimated using hysteresis observed after cloud transits. Based on a simple time-constant hysteresis model, we can correct for hysteresis in the IWC measurement. While it might be expected that this is a systematic error, lowering the ice water content measurement, we show in Part II that this depends on the specific cloud transit signature and could be positive when the total water signal is decreasing as the airplane is leaving the densest part of the cloud. Worst-case corrections range from –10% to +10% during a cloud encounter with an estimated uncertainty in the IWC measurement of 3% from hysteresis. There is also the possibility that hysteresis will impact the determination of ice water content in thin cirrus, when measurements in clear air just before and after the cloud show evidence of hysteresis. This can be accounted for by normalizing the clear-air signal to that of the water vapor instrument, but it requires the assumption that the degree of hysteresis changes smoothly through the cloud transect. While this cannot be strictly verified, it is only a concern when probing thin cirrus, where about 0.5 ppmv must be added to the overall uncertainty.

We next address item 1, maintenance of ambient particle concentration in the duct. Taking into account all the contributors to particle enhancement listed in Table 1 as previously described, we estimate a 15% uncertainty, leading to a total estimated 1-σ uncertainty of 18% in the ice water content of thick cirrus whose mass is dominated by particles greater than 20 μm. For thin cirrus or contrail encounters, where most of the ice mass is in small particles, the uncertainty might be marginally less.

These uncertainties include the potential systematic uncertainty of 5% from evaporation of ice particles in the water vapor duct but do not include the potential enhancement from large ice particles shattering off the

aircraft nose or the inlet diffuser. Regarding the former, a light trap in the water vapor duct has been shown from fluid flow calculations to have caused eddy formation with a resultant increase in residence time. This trap has been replaced with one exhibiting improved flow quality while maintaining sufficient light-trapping capability. Regarding the latter, while intercomparisons with the CLH instrument during CRYSTAL FACE and the MidCIX campaign show no evidence of enhancement from the shattering of large ice particles, comparisons with other ice water measurements with and without the diffuser would be helpful.

8. Conclusions

In this paper we have described the design and calibration of a total water instrument that when combined with simultaneous water vapor measurements from the Harvard photofragment fluorescence hygrometer will provide ice water mixing ratios with an estimated 1-σ uncertainty of 18%. Aside from uncertainties in the maintenance of ambient particle concentration in the duct, the three main sources of error in water measurement arise from uncertainties in the laboratory calibration, uncertainties in the validity of the laboratory calibration in flight, and contamination of the ambient air sampled at the instrument detection axis. The accuracy of both water instruments depends on the quality of the laboratory calibrations. By using the combination of added water as calculated by Eq. (3) and absorption at Lyman-α we minimize the potential systematic errors that might be present when solely relying on either of the two methods for determining the calibration coefficients. In-flight diagnostics that include radial absorption measurements and clear-air intercomparisons of the two water instruments further increase our confidence in predicted measurement accuracy.

Acknowledgments. This work was supported by NASA Grants NAG5-8779, NAG1-01095, and NAG5-115487. The hard work, cooperation, and continued support of the entire NASA WB-57 flight staff are gratefully acknowledged. The QNX Corporation is acknowledged for their generous donation of operating system software used for the operation of the water vapor and total water instruments.

REFERENCES

Avallone, L. M., and A. G. Hallar, 2003: Measurements of ice water content in low-latitude cirrus clouds. *Eos, Trans. Amer. Geophys. Union,* **78** (Fall Meeting Suppl.), Abstract A22A-1044.

Brown, P. R. A., 1993: Measurements of the ice water content in cirrus using an evaporative technique. *J. Atmos. Oceanic Technol.,* **10,** 579–590.

——, and P. N. Francis, 1995: Improved measurements of the ice water content in cirrus using a total-water probe. *J. Atmos. Oceanic Technol.,* **12,** 410–414.

Engblom, W. A., and M. N. Ross, 2003: Numerical model of airflow induced particle enhancement for instruments carried by the WB-57F aircraft. Aerospace Rep. ATR-2004 (5084)-1, 23 pp.

Hallar, A. G., L. M. Avallone, R. L. Herman, B. E. Anderson, and A. J. Heymsfield, 2004: Measurements of ice water content in tropopause region Arctic cirrus during the SAGE III Ozone Loss and Validation Experiment (SOLVE). *J. Geophys. Res.,* **109,** D17203, doi:10.1029/2003JD004348.

Hallett, J., and G. A. Isaac, 2002: Aircraft icing in glaciated and mixed phase clouds. Preprints, *40th Aerospace Sciences Meeting and Exhibit,* Reno, NV, American Institute of Aeronautics and Astronautics, P 0677.

Hinds, W. C., 1999: *Aerosol Technology: Properties, Behavior, and Measurement of Airborne Particles.* 2d ed. John Wiley and Sons, 483 pp.

Hintsa, E. J., E. M. Weinstock, J. G. Anderson, R. D. May, and D. F. Hurst, 1999: On the accuracy of in situ water vapor measurements in the troposphere and lower stratosphere with the Harvard Lyman-α hygrometer. *J. Geophys. Res.,* **104** (D7), 8183–8190.

Kelly, K. K., M. H. Proffitt, K. R. Chan, M. Loewenstein, J. R. Podolske, S. E. Strahan, J. C. Wilson, and D. Kley, 1993: Water vapor and cloud water measurements over Darwin during the STEP 1987 tropical mission. *J. Geophys. Res.,* **98** (D5), 8713–8723.

King, W. D., 1984: Air flow and particle trajectories around aircraft fuselages. I: Theory. *J. Atmos. Oceanic Technol.,* **1,** 5–13.

——, 1985: Air flow and particle trajectories around aircraft fuselages. III: Extensions to particles of arbitrary shape. *J. Atmos. Oceanic Technol.,* **2,** 539–547.

——, D. E. Turvey, D. Williams, and D. J. Llewellyn, 1984: Air flow and particle trajectories around aircraft fuselages. II: Measurements. *J. Atmos. Oceanic Technol.,* **1,** 14–21.

Kley, D., 1984: Ly(α) absorption cross-section of H_2O and O_2. *J. Atmos. Chem.,* **2,** 203–210.

——, J. M. Russell III, and C. Phillips, Eds., 2000: SPARC assessment of upper tropospheric and stratospheric water vapour. World Climate Research Programme Rep. 113, 312 pp.

McFarquhar, G. M., P. Yang, A. Macke, and A. J. Baran, 2002: A new parameterization of single scattering solar radiative properties for tropical anvils using observed ice crystal size and shape distributions. *J. Atmos. Sci.,* **59,** 2458–2478.

Murphy, D. M., and M. E. Schein, 1998: Wind tunnel tests of a shrouded aircraft inlet. *Aerosol Sci. Technol.,* **28,** 33–38.

Rader, D. J., and V. A. Marple, 1988: A study of the effects of anisokinetic sampling. *Aerosol Sci. Technol.,* **9,** 283–299.

Schiller, C., and Coauthors, 1999: Ice particle formation and sedimentation in the tropopause region: A case study based on in situ measurements of total water during POLSTAR 1997. *Geophys. Res. Lett.,* **26,** 2219–2222.

Scott, S. G., T. P. Bui, K. R. Chan, and S. W. Bowen, 1990: The meteorological measurement system on the NASA ER-2 aircraft. *J. Atmos. Oceanic Technol.,* **7,** 525–540.

Soderman, P. T., N. L. Hazen, and W. H. Brune, 1991: Aerodynamic design of gas and aerosol samplers for aircraft. NASA Tech. Memo. 103854, 13 pp.

Stephens, G. L., and Coauthors, 2002: THE CLOUDSAT mission and the A-TRAIN. *Bull. Amer. Meteor. Soc.,* **83,** 1771–1790.

Stocker, T. F., and Coauthors, 2001: Physical climate processes and feedbacks. *Climate Change 2001: The Scientific Basis,* J. T. Houghton et al., Eds., Cambridge University Press.

Twohy, C. H., A. J. Schanot, and W. A. Cooper, 1997: Measurement of condensed water content in liquid and ice clouds using an airborne counterflow virtual impactor. *J. Atmos. Oceanic Technol.,* **14,** 197–202.

Webster, C. R., and A. J. Heymsfeld, 2003: Water isotope ratios D/H, 18O/16O, 17O/16O in and out of clouds map dehydration pathways. *Science,* **302,** 1742–1745.

——, R. D. May, C. A. Trimble, R. G. Trave, and J. Kendall, 1994: Aircraft (ER2) laser infrared absorption spectrometer (ALIAS) for in-situ stratospheric measurements of HCl, N_2O, CH_4, NO_2, and HNO_3. *Appl. Opt.,* **33,** 454–472.

Weinstock, E. M., J. J. Schwab, J. B. Nee, M. J. Schwab, and J. G. Anderson, 1990: A cryogenically cooled photofragment fluorescence instrument for measuring stratospheric water vapor. *Rev. Sci. Instrum.,* **61,** 1413–1432.

——, and Coauthors, 1994: New fast response photofragment fluorescence hygrometer for use on the NASA ER-2 and the Perseus remotely piloted aircraft. *Rev. Sci. Instrum.,* **65,** 3544–3554.

——, J. B. Smith, D. Sayres, J. V. Pittman, N. Allen, and J. G. Anderson, 2006: Measurements of the total water content of cirrus clouds. Part II: Instrument performance and validation. *J. Atmos. Oceanic Technol.,* **23,** 1410–1421.

Zöger, M., and Coauthors, 1999: Fast in situ stratospheric hygrometers: A new family of balloon-borne and airborne Lyman α photofragment fluorescence hygrometers. *J. Geophys. Res.,* **104,** 1807–1816.